Diffusive Homeostasis in a Self-Organizing Recurrent Neural Network

Spatially dependent Interaction as a Determinant of Neural Activity and Plasticity

October 18, 2016

1 Abstract

Based on the LIF-SORN-model proposed in [1], we attempted to replace the intrinsic homeostatic control system used in the original version by a mechanism based on the diffusion of a neurotransmitter across the nervous tissue. The model of diffusive homeostasis was adopted from a paper by Y. Sweeney et al. [2] and models the tissue as a surface of square shape and a set of points on this surface, representing the neurons' positions within the SORN. The group of excitatory neurons then acted as a point-source of nitric oxide (NO), as well as as a sensor for the NO-concentration at each individual position. The production and sensing of NO forms the basis of a feedback loop: The individual NO-readout is fed into a comparator which causes an appropriate change within the internal firing threshold of the neuron, in turn altering the neuron's firing rate. The control system is then closed by linking the rate of NO-production to the neuron's firing rate.

Key aspects of this thesis include an analysis of the stability of the homeostatic control, followed by a comparison of features of the original LIF-SORN and the Diffusive variant. We expect to observe a preservation of non-random features that have been found in the original LIF-SORN while incorporating a stronger variance within neural activity (as reported by [2]) which has previously been suppressed by a rigid single-cell homeostasis. In the face of possible *new* features within the network's structure, one should further clarify the - presumably indirect - causal relation between diffusive spatial interaction and synaptic topology.

2 Methods

2.1 Network Simulation

The Neural Network was simulated with the code used in [1], which makes use of the BRIAN spiking neural network simulator [3]. Thus, all following explanations regarding the simulation of neurons and mechanisms of synaptic plasticity are based on the methods described in the aforementioned paper.

Across a square area of $1000 \times 1000 \, \mu m$, 400 excitatory LIF neurons and 80 inhibitory LIF neurons where assigned random positions. Before the start of the simulation, all but recurrent excitatory synapses where randomly generated until a desired connection fraction was reached. The connection probability between two neurons was calculated

1

parameter	EE	EI	IE	II
connection fraction	$\to 0.1$	0.1	0.1	0.5
initial connection strength	$0.0001mV$	$1.5mV$	$-1.5mV$	$-1.5mV$
conduction delay	$1.5ms$	$0.5ms$	$1.0ms$	$1.0ms$

Table 1: Parameters of synaptic connections.

from a distant dependent Gaussian function with a standard deviation of 200 μm. For exc. to inh. (EI) and inh. to exc. (IE) synapses, the connection fraction was set to 0.1, and 0.5 for recurrent inh. synapses (II). These connections where kept at a fixed connection strength throughout the simulation. Furthermore, all synapses where simulated with a fixed (distance independent) conduction delay. See table 1 for a summary of parameters.

Recurrent excitatory synapses where subject to a number of plastic mechanisms to be described in the following.

2.1.1 Synaptic Plasticity

Synaptic Growth: At a rate of 1/sec, the random, distance dependent generation of new EE synapses was carried out n times, where n is taken from a normal distribution with mean 920 and standard deviation $\sqrt{920}$. This constant growth rate was tuned to achieve the desired target concentration of 0.1 (see 1).

Synaptic Pruning: At the same rate of 1/sec, EE synapses below a threshold of 0.000001 mV where removed, thus being added again to the set of "potential" connections from which the growth process draws new connections. Especially, they were temporarily excluded from STDP (see below).

Spike Timing Dependent Plasticity: An additive STDP rule was used as described e.g. in [4]. The change of weight between two neurons due to a pre- and postsynaptic spike (i → j) is defined as:

$$\Delta w_{ji} = \sum_k \sum_l W(t_j^l - t_i^k) \tag{1}$$

$$W(\Delta t) = A_+ exp(-\Delta t/\tau_+), \qquad \Delta t > 0 \tag{2}$$

$$W(\Delta t) = A_- exp(\Delta t/\tau_-), \qquad \Delta t < 0 \tag{3}$$

Indexes k and l refer to the kth and lth pre- and postsynaptic spike respectively. Parameters where chosen to approximate data from [5] and [6], namely $\tau_+ = 15ms$, $A_+ = 15mV$, $\tau_- = 30ms$ and $A_- = -7.5mV$. However, for the sake of reduction of computational effort, we used the "nearest neighbor" approximation, only calculating the effect of the most recent pre-post pair of spikes for potentiation and post-pre pair for depression, yielding roughly the same value as the full summation due to the fast decay times τ_+ and τ_- of the STDP-window.

Synaptic Normalization: Among other, experiments have suggested rescaling of synapses among individual postsynaptic neurons as a form of activity regulation in the brain: While preserving ratios of weights, the mean incoming connectivity is multiplicatively adjusted. While this general mechanism has been confirmed in many experiments, results differ regarding the question whether the target connectivity is dynamically changing in order to preserve a certain postsynaptic firing rate (homeostatic synaptic scaling), or whether it remains constant, effectively enforcing a synaptic normalization. Though the latter does not directly enforce a fixed level of activity, one can argue that in a balanced recurrent network, synaptic normalization still reduces the

probability of very high or low firing rates caused by an above- or below-average total synaptic input.

We implemented synaptic normalization by calling a function once per sec., updating each w_{ji} from neuron i to neuron j as follows:

$$w_{ji} \to w_{ji} \frac{w_{total}}{\sum_i w_{ji}} \qquad (4)$$

w_{total} was set to different values for each of the four types of connections between the excitatory and inhibitory pool of neurons. Except for the dynamically populated EE-synapses, these values could be directly set in accordance with the previously given parameters of desired mean individual connection strength, size of the presynaptic population and connection fraction, by calculating $w_{total} = w_{mean} \cdot N_{presyn.pop} \cdot p_{connect}$. This yielded $w_{total,EI} = 60mV$, $w_{total,IE} = -12mV$, $w_{total,II} = -60mV$. $w_{total,EE}$ was set to $40mV$, corresponding to a mean synaptic weight of $1mV$, given a targeted EE-connection fraction of 0.1 and a population of 400 excitatory neurons.

Short Term Plasticity: As an additional stabilization of network activity, a short term plasticity (STP) mechanism acting on recurrent excitatory connections was implemented as presented in [7]. It modulates the effective synaptic weights by multiplying the value stored in the weight matrix w_{ji} by two dynamic variables x and u, $w_{ji}^{effective} = w_{ji} \cdot x \cdot u$, each synapse owning a pair (x, u). The dynamics of these variables are given by:

$$\dot{x} = \frac{1-x}{\tau_d}, \ \dot{u} = \frac{U-u}{\tau_f} \qquad (5)$$

Furthermore, each presynaptic spike causes a change of x and u by

$$x \to x - x \cdot u, \ u \to u + U(1-u) \qquad (6)$$

If no spikes arrive, the system rests at $x \cdot u = U$. Otherwise, depending on the choice of τ_d and τ_f, one can achieve a weight modulation that is dominated by potentiation ($\tau_f \gg \tau_d$) or depression ($\tau_f \ll \tau_d$). As a rough approximation of the values that where experimentally observed [7], we chose $U = 0.04$, $\tau_d = 0.5s$ and $\tau_f = 2s$, giving it a tendency towards potentiation. However, one should keep in mind that for $U \in [0, 1]$, $x \cdot u \in [0, 1]$ always holds, thus the factor $x \cdot u$ has a generally diminishing effect. E.g., for our choice of variables, a poisson input with a constant rate achieves the best synaptic transmission at a rate of $\sim 4.5Hz$, corresponding to $x \cdot u \approx 0.2$. "Potentiation" in this context refers to the fact that stronger input strengthens synaptic transmission *compared* to close to zero incoming spikes.

2.1.2 Neuron Model

We used a leaky integrate-and-fire-model for all neurons in the network, whose dynamics are described by a stochastic differential equation:

$$dV = -\frac{V - E_l}{\tau_m} dt + \frac{\sigma}{\sqrt{\tau_m}} dW \qquad (7)$$

where V is the membrane potential, E_l is the equilibrium membrane potential, τ_m is the time constant of the membrane, σ is the standard deviation of the noise term and dW is the standard Wiener process. A neuron is said to spike when its membrane potential reaches the threshold voltage V_t. The voltage is then reset to V_r. A refractory period was not implemented. A presynaptic spike causes a simple (delayed, see Table 1) increment of the membrane potential of the postsynaptic neuron by $w_{ji}^{effective}$. Table 2 summarizes the aforementioned set of parameters.

3

parameter	exc. neur.	inh. neur.
E_l	-60 mV	-60 mV
τ_m	20 ms	20 ms
V_r	-70 mV	-60 mV
σ	$\sqrt{5}$ mV	$\sqrt{5}$ mV
V_t	subject to IP	-58 mV

Table 2: Parameters of LIF neuron

2.1.3   Intrinsic Plasticity (IP)

Apart from dynamic processes within synapses which contribute to a stabilization of the network's activity, neurons possess internal mechanisms capable of maintaining a desired regime of activity. Regular-spiking cells are known to down-(up-)regulate their firing rate upon increased (decreased) input on a timescale of tens of milliseconds [8,9]. Since our simulation did not incorporate any rapidly changing external drive, the network itself was not expected to exhibit fast changes of synaptic input, allowing us to neglect this feature. On the other hand, a similar form of adaption as a reaction on deprived or enhanced input can be observed on a timescale of hours to days [10]. In contrast to the former short-term adaption, which can be explained by a separation of timescales among different ionic currents in the cell [11, p. 252-256], in the latter case, [10] finds evidence that a long-term change in excitability can be attributed to an altered resistance of ionic channels.

In the original LIF-SORN, a simple form of low intrinsic homeostasis was implemented by altering the neurons' firing threshold based on the deviation from a target firing rate. This thesis implemented a new model of slow intrinsic homeostasis, based on the work in [2]. The following section describes both models in further detail.

2.1.4   Modelling of Homeostatic Intrinsic Plasticity

Our original model of homeostatic control was described as an operation over discrete time steps $\Delta t = 0.1 ms$, carried out for each excitatory neuron:

$$V_t \rightarrow V_t + \eta_{IP}(N_{spikes} - h_{IP}) \tag{8}$$
$$N_{spikes} \rightarrow 0 \tag{9}$$

where V_t is the firing threshold, η_{IP} an adaption rate and h_{IP} the desired number of spikes per time step. N_{spikes} is a variable, counting the number of spikes of the neuron within each interval. In a continuous, rate-based form, this update rule can as well be written as:

$$\dot{V_t} = \eta_{IP}(r - r_{IP}) \tag{10}$$

with r as the neuron's firing rate and $r_{IP} = h_{IP}/\Delta t$ the target firing rate. This feedback control indirectly drives the firing rate of each neuron towards r_{IP}: If $r > (<)r_{IP}$, V_t increases (decreases), reducing (increasing) the probability of a spike to occur.

The model presented in [2] includes spatial interaction across excitatory neurons through the diffusion of nitric oxide (NO). Enzymes that are responsible for NO synthase (NOS) are present in different areas of the body, namely being involved in the dilation of blood vessels (endothelial NOS, eNOS) , the immune system (inducible NOS, iNOS) and the CNS (neuronal NOS, nNOS) [12]. These Enzymes differ in their functionality

and dependence on the presence of other molecules. In particular, nNOS is sensitive to the concentration of Ca^{2+} ionic Calcium [13].

Due to a depolarization of the membrane potential in the course of an action potential, voltage dependent Ca^{2+}-channels open, which causes a significant increase of the intracellular Calcium concentration (relative to the low concentration at rest) [14, p. 98-100]. A common theoretical description of voltage-dependent ion channels is provided by the Goldman-Hodgkin-Katz equations, see [14, p. 445-451]. As such, Ca^{2+} constitutes a causal link between spiking activity and the production of NO.

On the other hand, experimental studies have suggested that NO can act as a diffusive signalling pathway, decreasing intrinsic excitability [15], or generally suggest a role of NO in maintaining a functional state of activity [16].

Sweeney et al. combined these empirical findings into a model of *diffusive homeostasis*, which is governed by the following equations:

$$\dot{Ca^{2+i}}(t) = -\frac{Ca^{2+i}}{\tau_{Ca^{2+}}} + Ca^{2+}_{spike} \sum_j \delta(t - t^i_{spike,j}) \tag{11}$$

$$\dot{nNOS^i}(t) = \frac{1}{\tau_{nNOS}} \left(\frac{Ca^{2+i^3}}{Ca^{2+i^3} + 1} - nNOS^i \right) \tag{12}$$

$$\dot{NO}(\mathbf{r},t) = -\lambda NO + D\nabla^2 NO + \sum_i \delta^2(\mathbf{r} - \mathbf{r}^i_{neur}) \cdot nNOS^i \tag{13}$$

$$\dot{V}^i_t(t) = \frac{NO(\mathbf{r}^i_{neur},t) - NO_0}{NO_0 \cdot \tau_{V_t}} \tag{14}$$

A depolarization within a nerve cell upon a spike-event t_{spike} causes a fixed inflow of ionic current Ca^{2+}_{spike}, which is modelled as an instantaneous increase of the Ca^{2+} concentration. Over time, the concentration decays exponentially by a time constant $\tau_{Ca^{2+}}$, see (11). Though Ca^{2+} currents can be described in a much more detailed fashion, it can be considered as a reasonable approximation [17, p. 198-203]. The aforementioned influence of Ca^{2+} onto nNOS was modelled by Sweeney et al. through (12), using the Hill equation [18] to model a cooperative binding mechanism. The $nNOS$ production is then fed into the "pool" of nitric oxide via point sources located at the neurons' positions. Apart from the inflow and the diffusive term $D\nabla^2 NO$, an additional decay term was added to provide a stable finite NO concentration under constant neuronal activity.

Finally, the dynamics of the firing thresholds V^i_t were modelled such that the rate of change is proportional to the relative deviation of the NO concentration at the neurons' locations from a global target concentration NO_0.

Obviously, the appropriate choice of NO_0 is crucial for the goal of achieving and maintaining a certain level of activity. However, one cannot directly set a parameter of the model to the desired population activity, as it was the case for canonical intrinsic homeostasis. Rather, one needs to determine the average concentration *associated* with the desired activity and set it as a target concentration. Though it is possible to derive this relation in an analytic fashion, for practical purposes of the simulation, we let the system run with the previous homeostatic mechanism, still solving equation (11)-(13) until a steady mean over the concentrations at the neurons' positions was reached. This mean was then set to be the target concentration and we switched to diffusive homeostasis. Table 3 summarizes the choice of parameters that where introduced in this section.

parameter	value
r_{IP}	3 Hz
η_{IP}	0.1 mV
Ca^{2+}_{spike}	1
$\tau_{Ca^{2+}}$	10 ms
τ_{nNOS}	100 ms
D	default: 12500 $\mu m^2 s^{-1}$
λ	0.1 s^{-1}
τ_{V_t}	see section 3.1

Table 3: Parameters of homeostatic intrinsic plasticity.

2.2 Simulation of Diffusion

We solved (13) with the finite difference method on a grid with a resolution of 100×100 points. Integration over time was carried out by a 4th-order Runge-Kutta method with a time step of $1ms$. On each time step, $\nabla^2 NO(\mathbf{r})$ was approximated by

$$\nabla^2 NO(\mathbf{r}_{i,j}) \approx \frac{NO_{i+1,j} + NO_{i-1,j} + NO_{i,j+1} + NO_{i,j-1} - 4NO_{i,j}}{h^2} \qquad (15)$$

where $h = L/100$ is the distance between neighboured grid points, determined by the length L of the square sheet and the resolution of the numeric grid. We implemented three possible boundary conditions into the simulation:

1.) Periodic boundary conditions:

$$NO_{i,N+1} = NO_{i,0} \qquad (16)$$
$$NO_{N+1,i} = NO_{0,i} \qquad (17)$$
$$NO_{i,-1} = NO_{i,N} \qquad (18)$$
$$NO_{-1,i} = NO_{N,i} \qquad (19)$$

with N being the grid resolution.

2.) Neumann boundary conditions, with $\nabla NO = (0,0)$ at the boundaries:

$$NO_{i,N+1} = NO_{i,N-1} \qquad (20)$$
$$NO_{N+1,i} = NO_{N-1,i} \qquad (21)$$
$$NO_{i,-1} = NO_{i,1} \qquad (22)$$
$$NO_{-1,i} = NO_{1,i} \qquad (23)$$

3.) Dirichlet boundary conditions, with $NO = NO_{bound}$ at the boundaries.

If not explicitly marked differently, Neumann boundary conditions where used for most of the simulations. This decision relates to the previously described mechanism of synaptic growth: Neurons placed close to the edge of the sheet have a lower connection probability due to the absence of neighbouring neurons in the direction perpendicular to the close-by border. It therefore models the synaptic growth within a square "cutout" of neural tissue. The Neumann boundary condition fits into this picture, since it allows a zero-flux condition at the borders. This is a reasonable assumption, because NO molecules cannot diffuse out of the tissue (unless they were placed in a fluid surrounding).

Equation (13) describes the influx of NO as a sum of scaled and spatially shifted Dirac functions. Apart from the question, whether this source term results in a well defined, finite solution at the neurons' positions (see section !!??!!), it can only be modelled to a certain degree of accuracy, depending on the resolution of the numeric grid. In practice,

we approximated the point sources of NO as an insertions at individual grid cells at a rate of $nNOS^i(t)/h^2$, where the normalizing divisor h^2 ensured the desired total influx per neuron. This numeric implementation required two additional constraints: First, all random neuron positions were confined to integer multiples of h in x- and y-direction. Second, to avoid redundancy and for physiological reasons, each grid cell could only hold one neuron at maximum. Both conditions combined led to an iterative generation of positions, where for each neuron a random number generator produced pairs of integers (n_x, n_y), each within $[0, N]$, until an unoccupied pair of integers was found and occupied, moving on to the next neuron. Figure 1 shows an example of the resulting NO density.
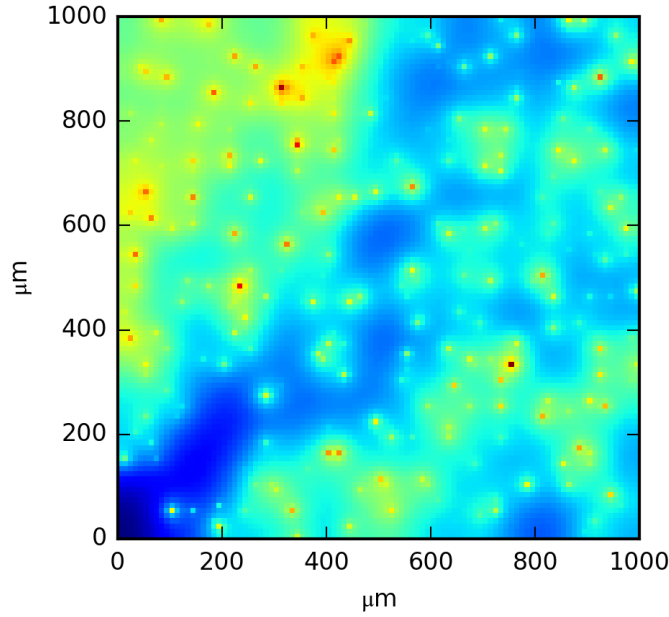
Figure 1: Example of NO-diffusion with 400 point sources of excitatory neurons.

3   Results

Since our main goal of the implementation of diffusive homeostasis was to allow the network to develop a broader distribution of firing rates across excitatory neurons compared to the original version of homeostasis, we first present the results of a comparison between features of the network activity in both variants in section 3.1. Following this is an analytic discussion of an instability we observed within the diffusive homeostatic feedback loop, see section 3.2. Furthermore, we compare topological features of the network under the influence of diffusive and non-diffusive homeostasis in section ???.

3.1   Activity Analysis

As a first attempt, we set the time constant of threshold adaptation in the diffusive homeostasis to $2500\,\mathrm{ms}$, as given by [2]. Switching between non-diffusive/diffusive homeostasis after 700 seconds, Figure 2 shows the resulting dynamics of the population activity of the

excitatory and inhibitory group, the average NO concentration at the excitatory neurons' positions and the average firing threshold within the exc. group (inh. threshold was fixed, see table 2). Both homeostatic mechanisms managed to keep the excitatory population activity in the desired range of 3 Hz. However, what might appear to be slightly faster and stronger random fluctuations in the upper three plots of Figure 2, are in fact regular oscillations across all three depicted variables. While the oscillation amplitudes undergo a rather unpredictable time course, the frequency remains at a constant level of $\simeq 0.5\,Hz$. Although one might argue that - for the sake of practical purposes - regular oscillations of the NO concentration are not of much concern for the network as such, a periodically fluctuating firing rate is a qualitative feature requiring further inquiry.

Rhythmic patterns of activity are a commonly observed phenomenon within the brain. Depending on the rate of oscillations, the location within the brain and the spatial scale over which they are observed, different physiological features are found to be responsible, leading to explanatory models at different levels of abstraction. On a microscopic, single-neuron level, a so-called slow after-hyperpolarization conductance explains the appearance of bursting behaviour: A relatively short period of spiking activity is followed by a longer period of silence. This phenomenon can be modelled by a Ca^{2+}-dependent K^{+}-conductance. Upon the bursting period, Ca^{2+} concentration rises, prohibiting continuous spiking due to the activation of K^{+} current until the Ca^{2+} concentration has returned to base-level [17, p. 203-207]. However, due to the simplicity of our neuron model, this type of oscillating activity can be ruled out as an explanation.

On a larger, rate-based level, dynamical models of interconnected excitatory and inhibitory groups can exhibit sustained oscillations of activity [17, p. 270]. As a simplest model, one can describe the dynamics of the exc. and inh. populations as a 2-dimensional dynamical system, representing the respective population rates r_e and r_i:

$$\tau_e \dot{r}_e = -r_e + \phi_e(r_e W_{ee} + r_i W_{ie}) \tag{24}$$

$$\tau_i \dot{r}_i = -r_i + \phi_i(r_e W_{ei} + r_i W_{ii}) \tag{25}$$

where τ_e and τ_i represents time constants representing the rapidity of firing rate adaptation, ϕ_e and ϕ_i the respective transition functions between synaptic input and firing rate and W_{xy} the mean synaptic weight from population x to population y. A persistent oscillation then corresponds to a stable limit cycle in the 2-dimensional phase plane. According to the Poincaré-Bendixson Theorem, such a limit cycle exists inside a region R if R contains no fixed points and if any trajectory whose starting points lies within R is confined to R. The second condition is equivalent to the condition that for all points $\mathbf{r}_{edge}$ on the edge of R, the vector field $\dot{\mathbf{r}}_{edge}$ is facing "into" R, see [19, p. 248]. This case occurs if the system has a locally unstable fixed point, but a non-linearity that prevents an infinite deviation from the fixed point. Coming back to the dynamics in question, one would need to show that the network has a locally unstable fixed point at $(r_e, r_i) \approx (3\,Hz, 13\,Hz)$, see A* in Figure 2. Several aspects come into play, making it a hard task to fit the full spiking network model onto the simplified equations 24 and 25. First, the choice of τ_e and τ_i in 24 and 25 has significant influence onto the stability of the system. However, a straightforward equivalent does not exist in the used spiking neuron model. It has been shown that in the case of slowly varying input $\tau_{e/i}$ of equation 24 and 25 are equal to the membrane constant τ_m of the LIF-neuron used in the network [20], see equation 7. A second problem is to choose a good estimate of the activation functions $\phi_{e/i}(\cdot)$. In the absence of noise in equation 7, the firing rate for a given constant total input J is

$$\phi(J) = \begin{cases} \frac{1}{-\tau_m ln(\frac{V_t - E_l - J\tau_m}{V_r - E_l - J\tau_m})} & \text{for } J\tau_m + E_l > V_t \\ 0 & \text{otherwise} \end{cases}. \tag{26}$$
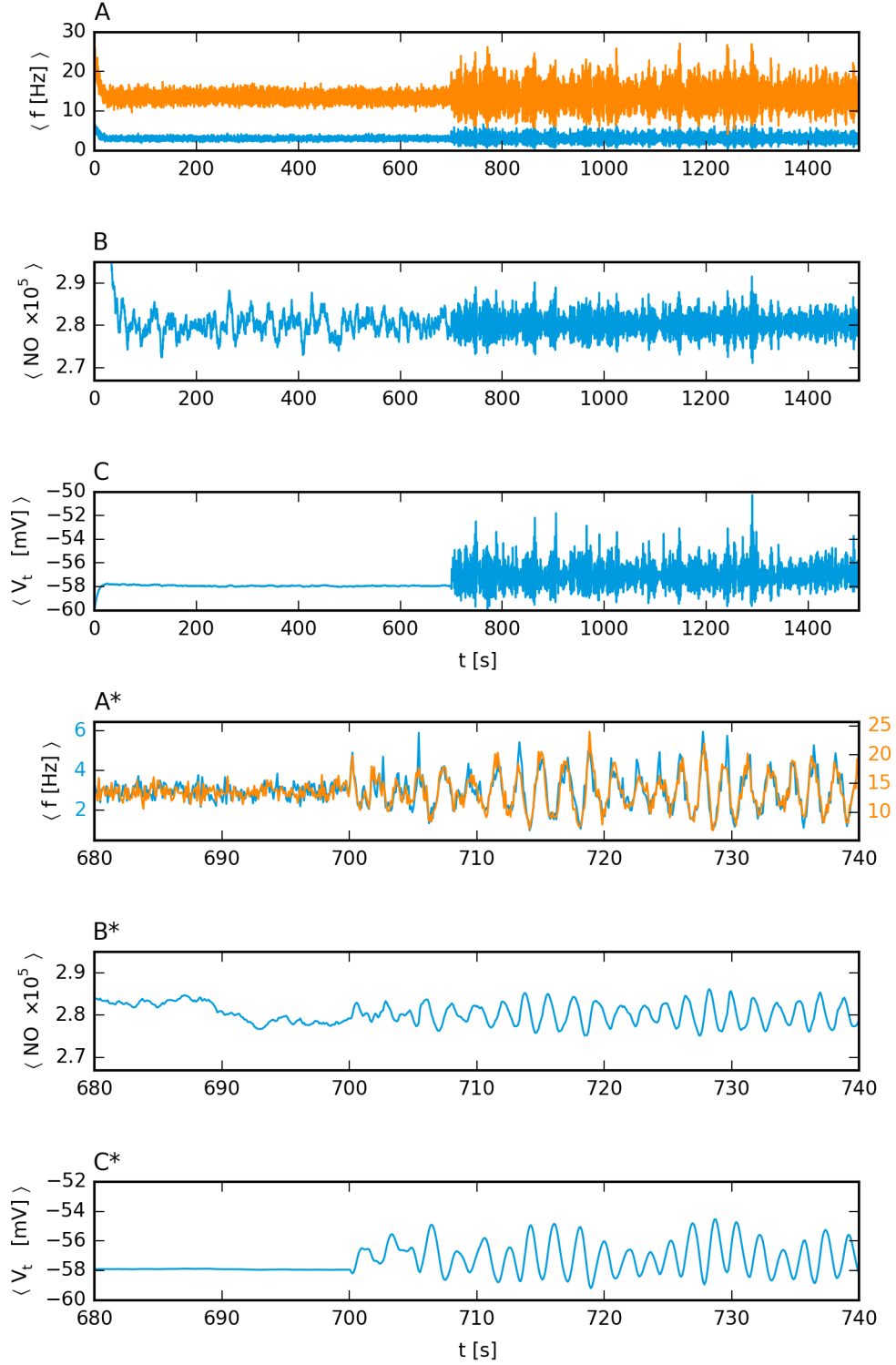
Figure 2: A/A*: Mean of excitatory (blue) and inhibitory (red) neuronal firing rate. B/B*: NO concentration averaged over readouts at exc. neurons' positions. C/C*: Average exc. firing threshold. Non-diffusive homeostasis was used for $0 - 700\,\mathrm{s}$, diffusive h. for $700 - 1500\,\mathrm{s}$. Target activity was $3\,\mathrm{Hz}$.
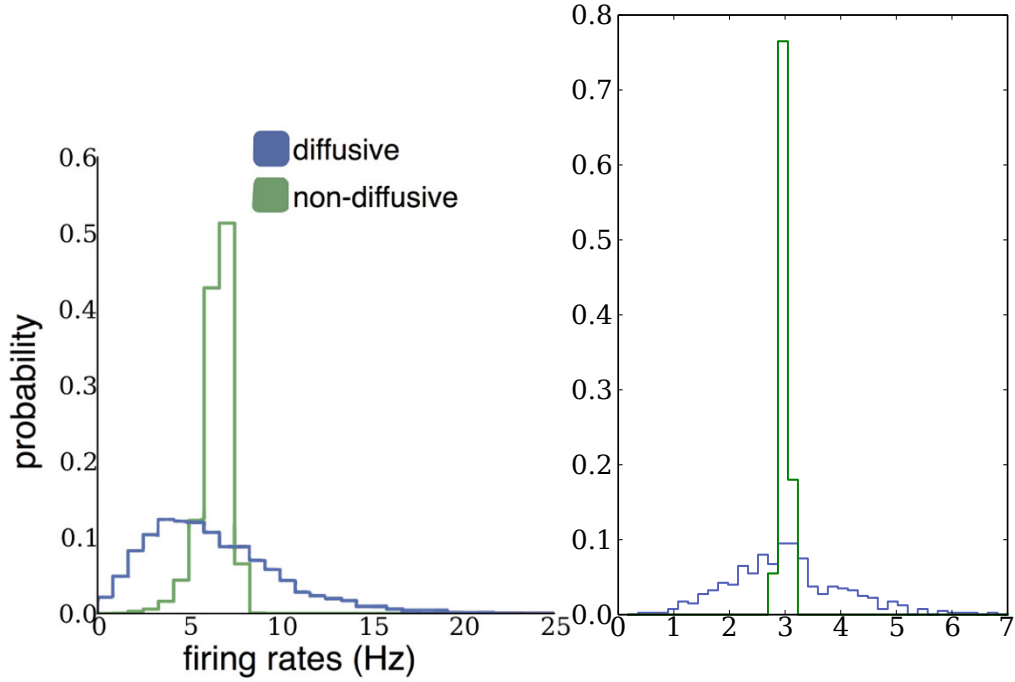
9

Figure 3: Left: Simulation results by Sweeney et al.. Right: Simulation results for the SORN.

As plot A* in Figure 2 indicates, the mean firing rates of both populations are highly correlated in time. For the source of oscillating behaviour to be found within the interaction between both populations,

A first approach in comparing the network activity before and after altering the homeostatic mechanism is by means of the distribution of firing rates within the network. As Sweeney et al. point out, it has been experimentally observed that firing rates are rather heterogeneous, resulting in a broad distribution. In Figure 3 we compare our results for the firing distribution to the results by Sweeney et al.. We observed a similar tendency of broader firing rate distributions for the diffusive homeostasis, though we did not get as heavy tailed statistics. Sweeney et al. found a reciprocal relation between the broadness of the firing rate distribution and the threshold distribution. The strong oscillations of the threshold make it difficult to estimate the threshold distribution in our case. For the plot in Figure 4, we calculated each neuron's time average threshold for the case of non-diffusive and diffusive homeostasis and used this as a basis for the distribution. In contrast to Sweeney et al., the statistics did not change significantly.

Another possibility of characterizing neural activity is to determine the distribution of interspike intervals (ISIs). Using non-diffusive homeostasis, one can observe a Poisson-like spiking behaviour with a stochastic refractory period, which is typically observed in cortical networks (This is not what can be observed for the case of diffusive homeostasis: the ISI distribution reveals preference of interspike times in the range of $1s$, whereas interspike times in of $0.1 - 0.6s$ are less likely than a Poisson process would predict. This deviation matches the frequency of activity oscillations, see Figure 2.

As a whole, the oscillating activity imposes a undesirable regularity onto the network's activity, see also Figure 6. While this effect might be tolerable without any external input, it is likely that the oscillations will overlay and obscure network responses onto external drive, presumably making it unusable for any computational task.
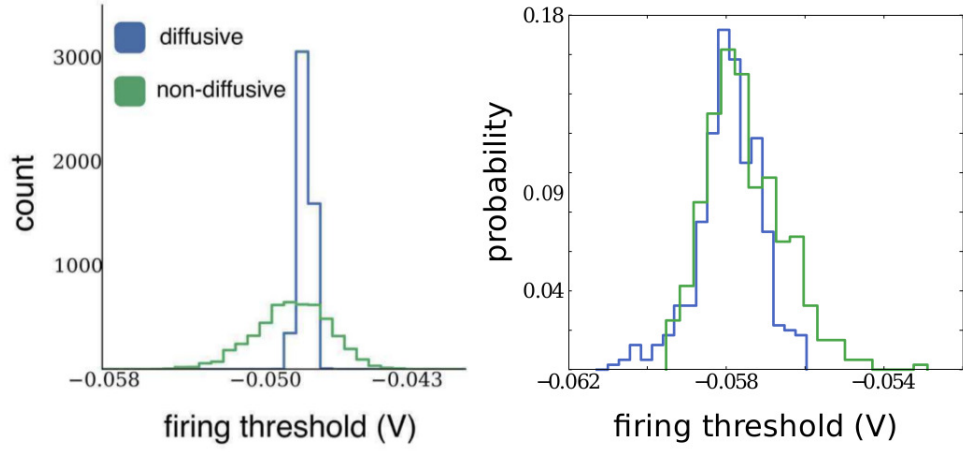
10

Figure 4: Comparison of threshold distributions observed by Sweeney et al. (left) and in the SORN (right).
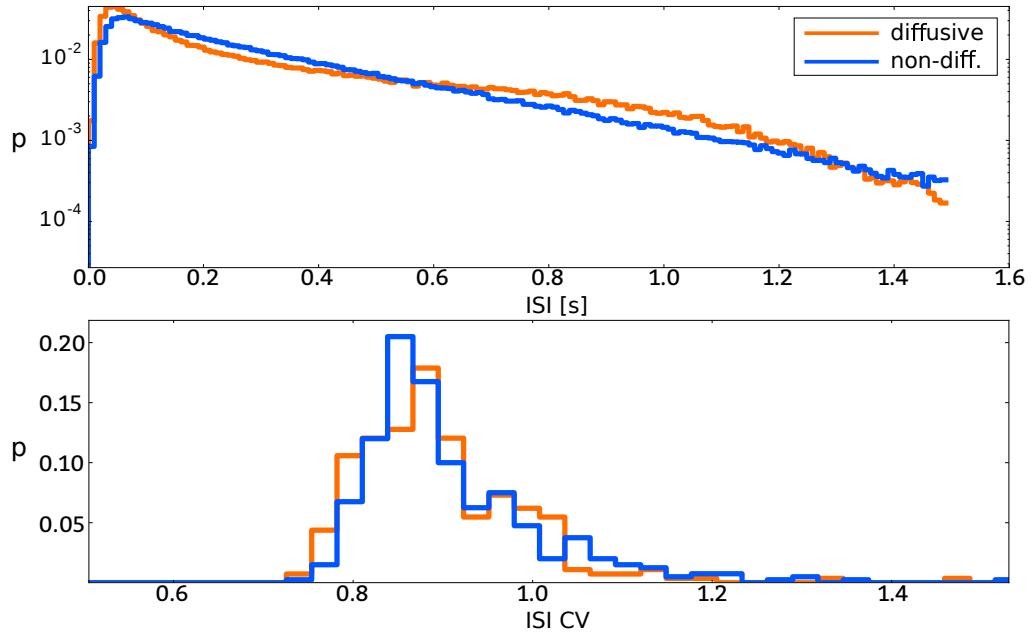

Figure 5: Top: log-plot of ISI-distribution of diff. and non-diff. homeostasis in the SORN. Bottom: CV-distribution for diff and non-diff. homeostasis.
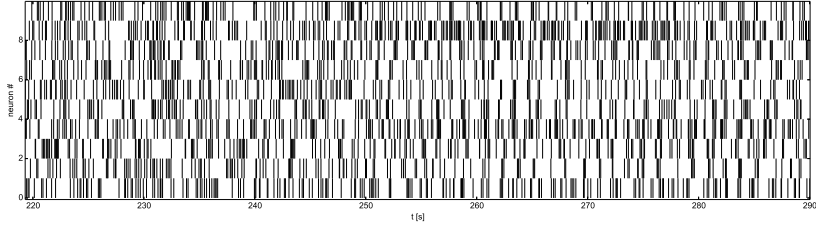
Figure 6: A spike sequence of 10 randomly picked excitatory neurons of the SORN. At $t = 250s$, the homeostatic mechanism is switched to the diffusive variant.

3.2   Analysis of Sustained Oscillations

To find an explanation for the described oscillations and a possible way of avoiding them, one has to find the necessary minimal set of mechanisms, required to explain the observed phenomenon, without oversimplifying crucial aspects of the minimal model. In our model, there are two aspects whose simplification is of particular importance: First, it is impossible to analytically predict every single spike within the entire network. Our analytical treatment therefore aims to find analytical expressions for momentary firing rates among the network. Second, one might speculate that the exact solution of the NO diffusion process can be simplified in favour of a model, where one describes the dynamics of the average NO concentration across the nervous tissue. This approach can be justified by the fact that a unified, average NO concentration is effectively equal to a very large diffusion rate.

We took several approaches to find the minimal set of equations that sufficiently reproduces the desired phenomena. Here, we will present the final and most successful version. We derived the equation from the following assumptions and results:

- Oscillations persisted for very large diffusion constants. Therefore, one may assume that the dynamics of NO solely depend on the decay rate λ and can be expressed by a single scalar variable.

- We observed that even though the overall activity oscillated, the total input for each neuron remained at a relatively steady level, only showing random fluctuations with periodically increasing and decreasing deviations. One can therefore assume that the effect of recurrent, "self-feeding" network dynamics can be neglected.

- The firing rate distribution has a significant variance.

- Since we simplified the NO dynamics to a global variable, all thresholds follow the same dynamics (apart from a variance in the initial conditions). We can therefore as well reduce the problem to a single average threshold variable.

- The phase difference between threshold and activity appears to be practically zero. It is therefore reasonable to assume a direct functional dependence $r_{pop} = r(\theta)_{pop}$.

- In the regime of the desired population activity of $3\ Hz$, nonlinearities within the "$spike \rightarrow Ca^{2+} \rightarrow nNOS$" mechanism can be neglected in favour of a simple relation $nNOS = C \cdot r_{pop}$.
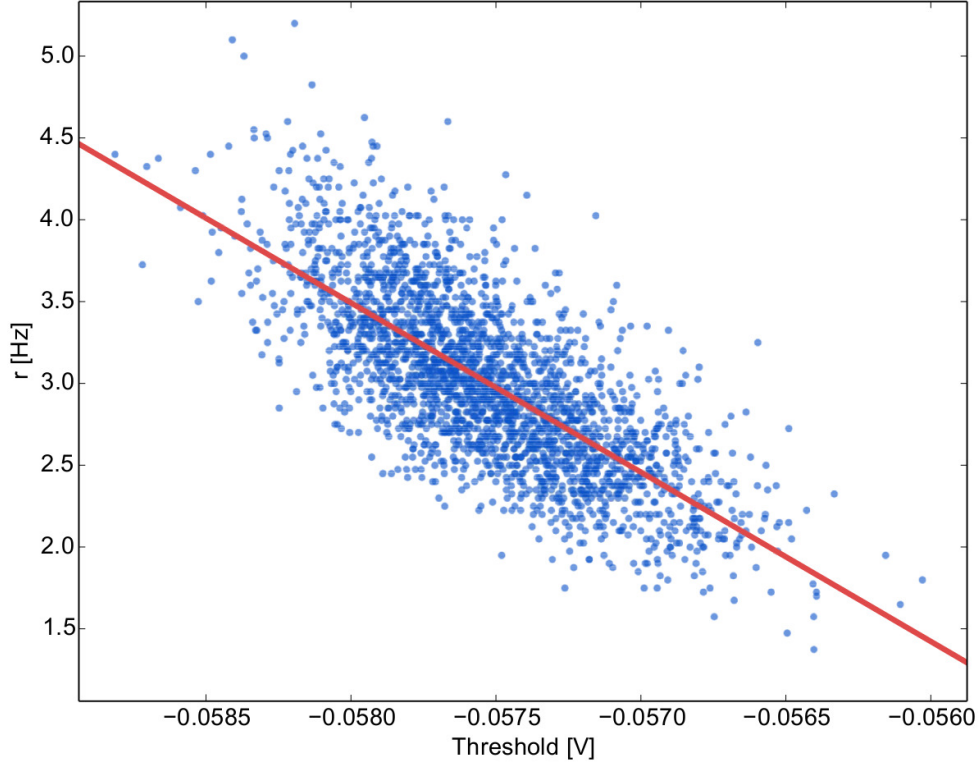
12

Figure 7: Linear fit of the relation between the firing threshold (averaged over population) and the population activity. $R^2 = 0.99996$.

These conclusions can be transferred into the following "simple" dynamical system:

$$\dot{NO} = -\lambda NO + C \cdot r(\theta) + C \cdot \sigma \xi(t) \tag{27}$$

$$\dot{\theta} = \frac{NO}{NO_0 \cdot \tau_\theta} \tag{28}$$

Here, $\xi(t)$ represents standard gaussian noise, accounting for the fact that, apart from the regular oscillation, the population activity features a certain amount of fluctuations. As an additional simplification, the fixed point was set to the origin.

To complete the expression, one has to find an appropriate description of the $r(\theta)$-relation. As a most simple approximation, we applied a linear regression to the data of the average threshold and the corresponding population activity, see Figure 7. The constant C in equation (27) is then proportional to the slope of the linear fit. In addition, C is proportional to the amount of NO released per spike, proportional to the number of contributing neurons and antiproportional to the total area of the tissue. We can solve and integrate equations (11) and (12) for a single spike, resulting in a total of $\tau_{Ca^{2+}} \cdot ln(1 + Ca_{spike}^{2+}{}^3)/3$. Therefore, $C = N_{neur} \cdot \tau_{Ca^{2+}} \cdot ln(1 + Ca_{spike}^{2+}{}^3)/(3 \cdot L^2)$ and $C \cdot r(\theta) = \theta \cdot \alpha \cdot N_{neur} \cdot \tau_{Ca^{2+}} \cdot ln(1 + Ca_{spike}^{2+}{}^3)/(3 \cdot L^2)$, where α is the slope of the linear fit and L^2 the area of the tissue. Figure 8 shows the results achieved from the simulation. We observe that noise is capable of maintaining oscillations in an otherwise stable linear system.

Is it possible to get a better understanding of the achieved dynamics? For that purpose, we note that equations (27) and (28) can be transformed into the following:
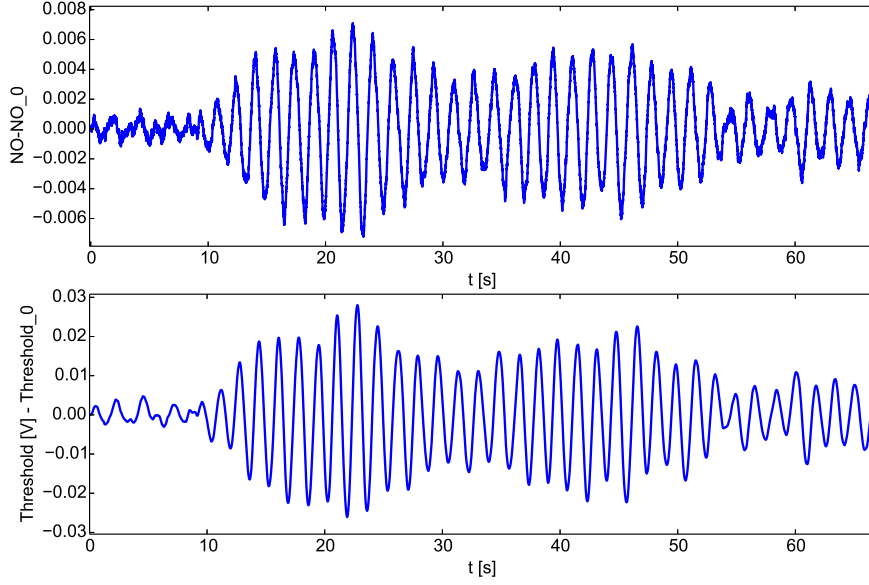
Figure 8: Simulation results for equations (27) and (28).

$$\dot{v} = -\frac{\lambda}{m}v - \omega_0^2 x + \frac{C \cdot \sigma}{m}\xi(t) \tag{29}$$

$$\dot{x} = v \tag{30}$$

with $x = \theta NO_0\tau_\theta$, $v = NO$, $m = 1$ and $\omega_0^2 = -\frac{\alpha C}{NO_0\tau_\theta}$. This set of equations is equal to a Langevin equation, describing a brownian particle in a harmonic potential. By taking the fourier transform of both equations, one can find an analytic expression for the power spectrum of the particle's location:

$$S_x(\omega) = \frac{S_\xi(\omega)}{(\omega_0^2 - \omega^2)^2 + \lambda^2\omega^2} \tag{31}$$

where, in the case of white gaussian noise, $S_\xi(\omega) = C^2 \cdot \sigma^2$. Substituting the transformations yields

$$S_\theta(\omega) = \left(\frac{C\sigma}{NO_0\tau_\theta}\right)^2 \frac{1}{(\frac{\alpha C}{NO_0\tau_\theta} + \omega^2)^2 + \lambda^2\omega^2} \tag{32}$$

By calculating the steady-state solution of equation (27), one can analytically express the target concentration NO_0 as a function of the desired pop. rate r_g:

$$NO_0 = r_g \frac{N_e \cdot \tau_{Ca^{2+}} \cdot ln(1 + Ca_{Spike}^{2+}{}^3)}{3\lambda L^2} = r_g\frac{C}{\lambda} \tag{33}$$

Substituting into equ. (32) one gets

$$S_\theta(\omega) = \frac{\sigma^2}{(\alpha + \frac{r_g\tau_\theta\omega^2}{\lambda}) + \tau_\theta^2 r_g^2\omega^2} \tag{34}$$
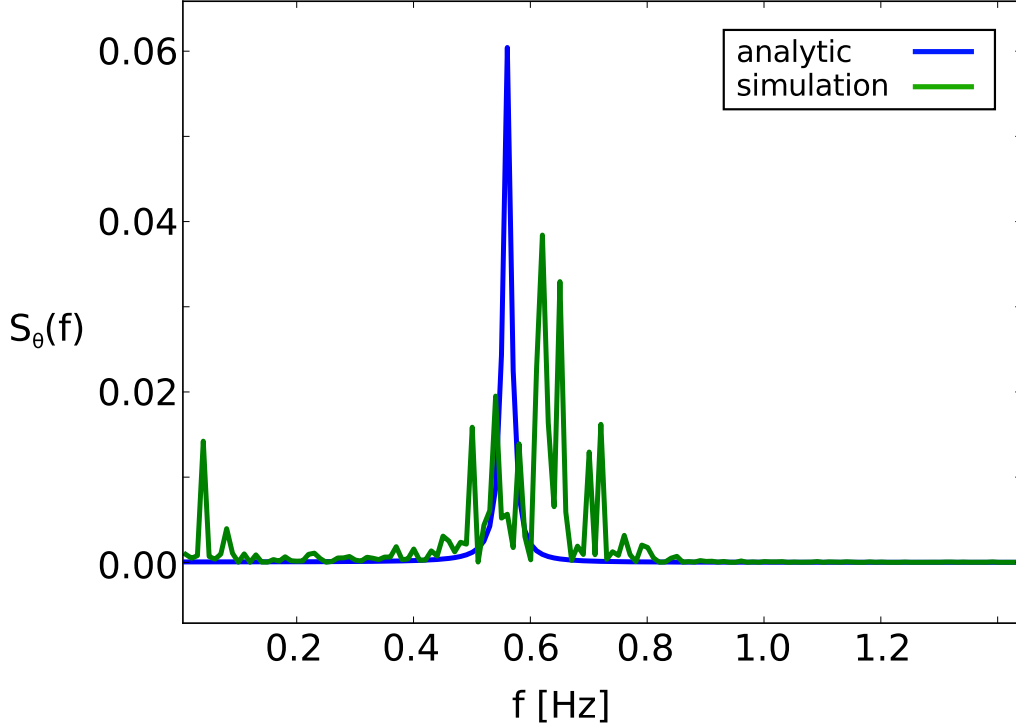
14

Figure 9: Power Spectrum of the firing threshold and analytic result of equation (34).

The maximum of this function then is

$$\omega_{max} = \sqrt{-\lambda(\frac{1}{2} + \frac{\alpha}{\tau_\theta r_g})} \tag{35}$$

$$S_\theta(\omega_{max}) = \frac{\sigma^2}{\tau_\theta^2 r_g^2 \left(\frac{1}{4} - \frac{\lambda}{2}\right) - \alpha\lambda\tau_\theta r_g} \tag{36}$$

Figure 9 suggests that the theoretical result does not fully cover the dynamics of the simulation, but supports the observation of a sustained oscillation at a preferred frequency.

For the purpose of reducing the oscillations to a negligible amplitude, λ and τ_θ can be increased. Note however that increasing λ will also increase ωmax, which will presumably result in faster oscillations. τ_θ on the other hand leads to a decrease of both, ω_{max} and $S_\theta(\omega_{max})$.

Since the $S_\theta(\omega)$ represents a spectral density, one should not directly relate $S_\theta(\omega_{max})$ to the actual squared amplitude of the oscillation. However, due to the linearity of the fourier transform, "rescaling" in the frequency spectrum also proportionally alters the amplitude of the signal in the time domain.

4   The Firing Rate Distribution in the Network

As shown in Figure 3, the distribution of firing rates within the population of neurons is highly dependent on the diffusion constant D, in accordance to the findings by Sweeney et. al. To analyze this dependence, a dynamic mean-field approach was suggested in [2]. In short, it consists of set of equations which need to be fulfilled self-consistently.

$$\nu = \langle \phi \rangle = \frac{\sum \phi_i}{N} \tag{37}$$

$$\phi_i = \phi_i(\mu_i(\nu), \sigma_i(\nu), \theta_i) \tag{38}$$

$$\mu_i = J_i C_i \nu \tau \tag{39}$$

$$\sigma_i = J_i \sqrt{C_i \nu \tau} \tag{40}$$

where ν is the mean population firing rate, ϕ_i the individual firing rate of neuron i, μ_i, σ_i and θ_i its synaptic input mean and standard deviation and intrinsic firing threshold respectively and J_i, C_i and τ the neuron's mean synaptic efficacy, number of incoming neurons and the membrane time constant. Self consistency is achieved by iterating through equations (37) and (38) until the desired precision is reached.

As a simplification, the authors of 3 proposed to implement diffusive homeostasis in this context by the following equation:

$$\frac{d\theta_i}{dt} = \frac{1}{\tau_{HIP}} \left((1 - \alpha) \frac{\phi_i - \phi_0}{\phi_i} + \alpha \frac{\langle \phi \rangle - \phi_0}{\langle \phi \rangle} \right) \tag{41}$$

$\alpha \, \epsilon \, [0, 1]$ thereby acts as a parameter that determines the "mixture" between single-neuron-homeostasis ($\alpha = 0$) and the limit of quasi instantaneous spreading of the diffusive signal across the population ($\alpha = 1$).

The authors claim that this model reproduces observations in the full network, namely that the steady-state firing rate distribution spreads out due to a larger diffusion constant (or a larger α, respectively).

However, in the following, I will argue that the steady-state solution of this simplified model will result in the same firing rate ϕ_0 for all neurons, no matter what α is set to. This can be seen by setting the left hand side of equ. (41) to 0 (which is necessarily the case in the steady state) and rearranging the equation:

$$(\alpha - 1) \frac{\phi_i - \phi_0}{\phi_i} = \alpha \frac{\langle \phi \rangle - \phi_0}{\langle \phi \rangle} \tag{42}$$

The right term of the equation is the same for all neurons i. Since the left term is monotonic as a function of ϕ_i, only one specific solution $\phi_i = \Phi$ for all i exists that equals the given term on the right. Furthermore, this implies $\langle \phi \rangle = \Phi$. Thus,

$$(\alpha - 1) \frac{\Phi - \phi_0}{\Phi} = \alpha \frac{\Phi - \phi_0}{\Phi} \tag{43}$$

which is only fulfilled for $\Phi = \phi_0$.

Moreover, one can argue that this result also implies a fixed distribution of thresholds in the steady state, independent of α: Given the result above, one finds

$$\phi(\mu_i(\nu), \sigma_i(\nu), \theta_i) = \phi_0 \tag{44}$$

$$\mu_i = J_i C_i \phi_0 \tau \tag{45}$$

$$\sigma_i = J_i \sqrt{C_i \phi_0 \tau} \tag{46}$$

$$\rightarrow \theta_i = \phi^{-1}(J_i C_i \phi_0 \tau, J_i \sqrt{C_i \phi_0 \tau}, \phi_0) \tag{47}$$

which implies that θ_i only depends on the given network topology.

In [2], a non-interacting population of neurons was simulated while inputs where drawn randomly from a gaussian distribution supposed to model the input statistics of the full network.

To verify our remarks concerning the dynamic mean field model, we simulated a similar population, but used an interacting population of neurons of the same size as in the previous simulations (400 excitatory, 80 inhibitory neurons). This allowed us to directly use a weight matrix acquired by means of a simulation of the full plastic network, taken from the network after $1500s$ (i.E., the "stable" phase). Individual values for μ_i and σ_i where then calculated according to (39) and (40). Note however that in this case the mean (input) firing rate ν also takes different values ν_i for each neuron.

Instead of directly iterating through equations (37) - (40) (as done in [2]) to fulfil self-consistency, we described the dynamics of the neurons' rates r_i through a continuous dynamic equation

$$\frac{dr_i}{dt} = \frac{1}{\tau_m}\left(-r_i + \phi_i(\mu_i(\nu), \sigma_i(\nu), \theta_i)\right) \tag{48}$$

where τ_m is the membrane time constant.

Of course, equation (37) has to be rewritten accordingly:

$$\nu_i = \langle r \rangle_{presyn.,i} \equiv \frac{\sum_{\exists syn.j \to i} r_j}{N_{presyn.,i}} \tag{49}$$

Figure 10 depicts the resulting dynamics for $\alpha = 0.4$ and $\alpha = 0.8$. Both predictions can be confirmed: All rates approach the same target rate of $3Hz$ and, apparently, thresholds move toward the same state for either choice of α. A significant difference only exists within the dynamics leading to the steady state. Roughly, a smaller value of α leads to a faster relaxation. Though, changes in the dynamics appear to be more subtle than a simple rescaling in the time domain.

4.1 Equilibrium in the full diffusive Model

Since the previous section has proven the simplified model in [2] to be incapable of maintaining a broad distribution of firing rates, turning to a more general formulation of the problem seems reasonable, especially if it includes the possibility of the "exact" description of the initial model.

Equation (13) describes the full dynamics of the diffusive neurotransmitter. Furthermore, equation (27) represents a simplification by means of two assumptions, namely the disregard of the diffusive term and the simplification of the process of NO-generation to a simple relation $nNOS_i = C \cdot r_i$, r_i representing a neuron's rate. Here we would like to discuss the implications of an "in-between" simplification, only applying the second one, but retaining the diffusive term:

$$\frac{dNO}{dt}(\mathbf{x}, t) = -\lambda NO + D\nabla^2 NO + \sum_i \delta^2(\mathbf{x} - \mathbf{x}_{neur,i}) \cdot C \cdot r_i \tag{50}$$

As in the previous section, we ask for the steady-state distribution of rates. Thus as a first step, one needs to solve

$$(\lambda - D\nabla^2)NO = \sum_i \delta^2(\mathbf{x} - \mathbf{x}_{neur,i}) \cdot C \cdot r_i \tag{51}$$

for $\{r_i\}$, such that

$$NO(\mathbf{x}_{neur,i}) = NO_0 \ , \ \forall i \tag{52}$$
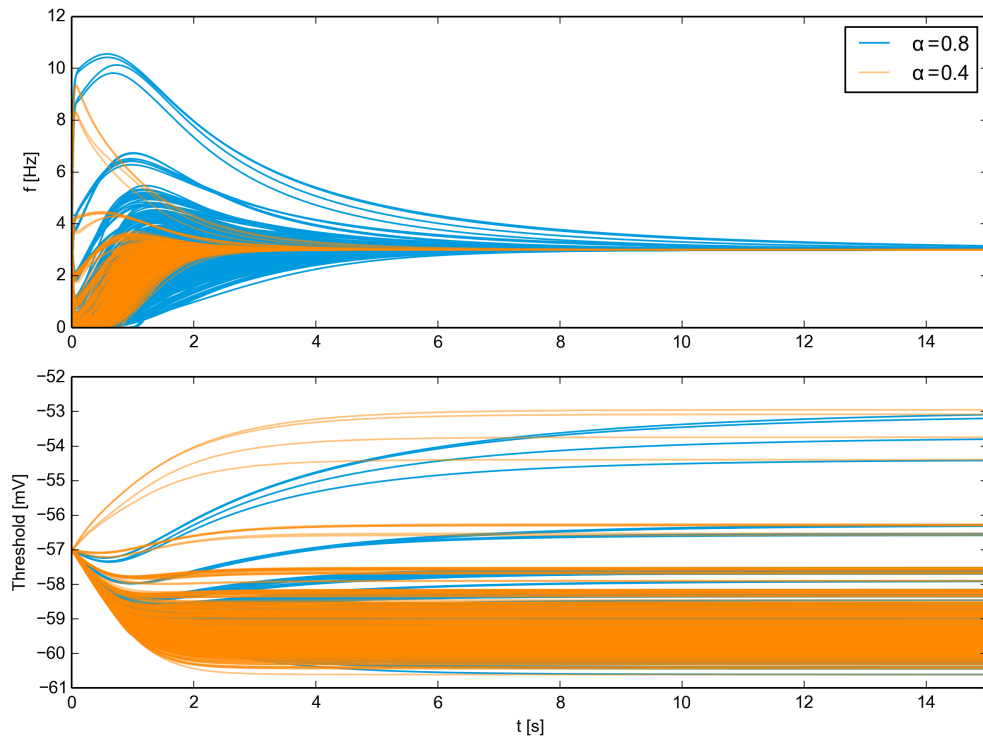
Equation (51) can be rewritten as

Figure 10: Dynamics of rates and thresholds of excitatory population of 400 Neurons (see equations (48) and (41)). For both values of α, rates and thresholds approach the same steady state.

$$\left(\nabla^2 + \left(i\sqrt{\frac{\lambda}{D}} \right)^2 \right) NO = \sum_i \delta^2(\mathbf{x} - \mathbf{x}_{neur,i}) \cdot \frac{-C \cdot r_i}{D} \tag{53}$$

Which is a two-dimensional Helmholtz equation with a superposition of (scaled) Dirac-functions. Thus, the solution of NO is composed of a superposition of shifted and scaled versions of the Green's function of the differential operator on the left of the equation. For each delta function $\delta^2(\mathbf{x} - \mathbf{x}_i)$, the solution is

$$NO_i(\mathbf{x}) = \frac{r_i C}{2\pi D} K_0 \left(|\mathbf{x} - \mathbf{x}_{neur,i}| \sqrt{\frac{\lambda}{D}} \right) \tag{54}$$

where K_0 is the zeroth modified Bessel function of the second kind. This solution reveals a fundamental problem of modelling the sources of NO-production as point sources: that is to say, the fact that $K_0(x)$ diverges to infinity for $x \to 0$. It is merely due to the finite density of the numeric grid used for the simulation of the diffusion that allows for a finite target value of concentration. Note that this problem only occurs in the two- or three-dimensional version of the differential equation, whereas in one dimension, the fundamental solution can be expressed as an exponential function with respect to the distance to the origin, resulting in a well-defined finite value at 0.

Generally speaking, no matter how the actual shape of the numeric solution in the equilibrium at a constant production rate will look like, it is expected to be of the form

$$NO_i(\mathbf{x}) = r_i \cdot \psi(d(\mathbf{x}_{neur,i}, \mathbf{x})) \tag{55}$$
$$d(\mathbf{x}, \mathbf{y}) \equiv |\mathbf{x} - \mathbf{y}| \tag{56}$$

The full solution is then

$$NO(\mathbf{x}) = \sum_i NO_i(\mathbf{x}) \tag{57}$$

If we define

$$\psi_{ij} = \psi_{ij} \equiv \psi(d(\mathbf{x}_{neur,i}, \mathbf{x}_{neur,i})) \tag{58}$$

we can express the condition (52) as

$$\sum_j \psi_{ij} \cdot r_j = NO_0 \tag{59}$$

or, as an operator

$$\hat{\psi}\mathbf{r} = NO_0 \mathbf{n} \tag{60}$$
$$\mathbf{n} \equiv (1, 1, ..., 1) \tag{61}$$

The problem of finding the steady-state solution of the homeostatic constraint thus reduces to inverting $\hat{\psi}$:

$$\mathbf{r} = NO_0 \hat{\psi}^{-1} \mathbf{n} \tag{62}$$

An example of a distribution of rates acquired from this method is shown in Figure 11.
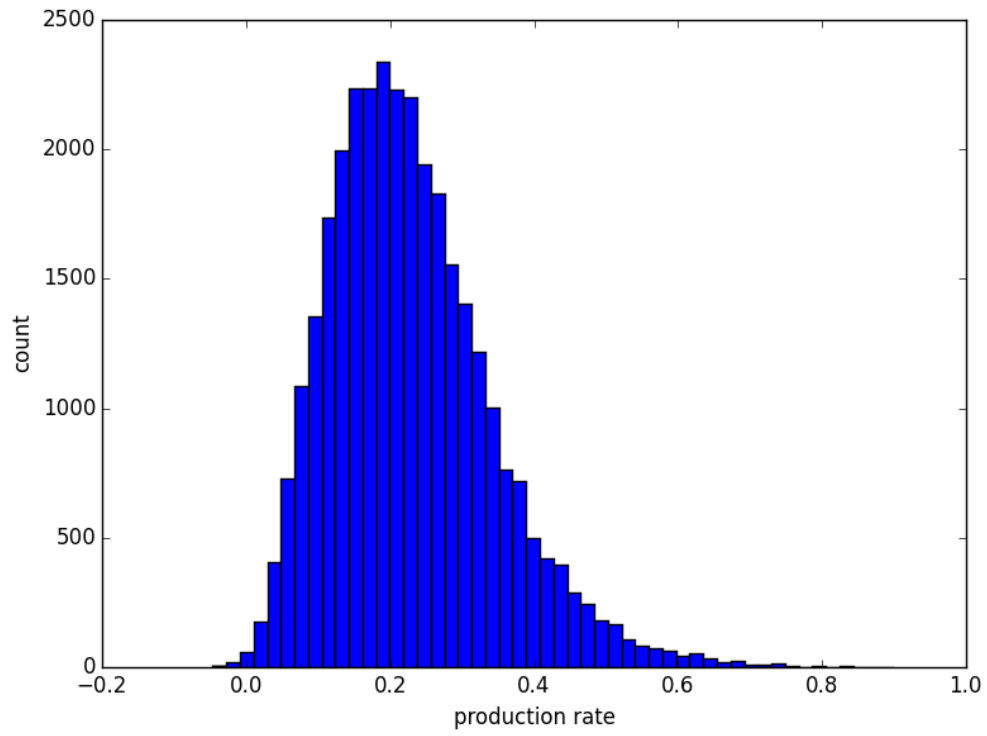
Figure 11: Distribution of the solution of (62) with an exponential distance dependent approximation in 2d (similar to the exact solution in 1d). For better statistical significance, calculations where carried out for 1600 random neurons-positions and 50 trials in total.

4.1.1 Results for an Approximation of the Numerical Steady-State Solution

If one aims for an appropriate expression for the numerical steady-state solution of a single "point"-source with a constant influx, two things should be of importance: first, it should correctly predict the concentration at the location of the source and second, it should be close to the analytic result in regions further away from the source. One possibility is to use the following "trick" to overcome the divergence of the analytic solution at the origin:

$$NO_{approx.}(d) = \frac{1}{\sqrt{\frac{1}{NO_{source,num.}^2} + \frac{1}{NO(d)^2}}} \tag{63}$$

At the pole $NO(0)$, $NO_{approx.}(0)$ then takes the value $NO_{source,num.}$. On the other hand, for larger values of r, the term $\frac{1}{NO_{source,num.}^2}$ becomes negligible compared to $\frac{1}{NO(d)^2}$, thus $NO_{approx.}(d) \rightarrow NO(d)$ for $d \rightarrow \infty$.

To find an approximation for $NO_{source,num.}$, one can interpret this value as a mean of the analytic solution across the square area covered by the corresponding grid cell. As an additional simplification, we substitute the necessary integration over the square grid cell by a circular area of equal size around the source. This calculation yields

$$NO_{source,num.} = r \cdot \frac{1 - h\sqrt{\frac{\lambda}{\pi D}}K_1\left(h\sqrt{\frac{\lambda}{\pi D}}\right)}{h^2\lambda} \equiv r \cdot \psi_{source,num.} \tag{64}$$

with r being the neuron's rate. Equivalently, one can then define

$$\psi_{approx.}(d) \equiv \frac{1}{\sqrt{\frac{1}{\psi_{source,num.}^2} + \frac{1}{\psi(d)^2}}} \tag{65}$$

4.1.2 Comparison of the Solution of the Random Matrix Equation and the Simulation of the Spiking Network

(63) and (64) can be used in (62) for a more accurate description of the distance-dependent diffusive interaction.

In addition, one needs to account for the boundary conditions used in the network simulation. We simulated the network with Neumann boundary conditions (setting the flux through the boundary to zero) as well as periodic boundaries. Both types can be modelled by extending the neurons' population through spatially shifted and mirrored versions of the base population (see Figure 12):

- Periodic boundary conditions are induced by copies of the neurons' positions shifted by $L \cdot (n_x, n_y)$, $n_x, n_y \in \mathbb{Z}$.

- Zero flux through the boundaries can be achieved by copied positions being shifted by $L \cdot (n_x, n_y)$, $n_x, n_y \in \mathbb{Z}$ *and* mirrored in $x(y)$-direction if $n_x(n_y)$ is odd.

The entries of the operator for periodic boundary conditions $\hat{\psi}_{per.}$ can now calculated by

$$\psi_{ij,per.} = \sum_{n_x,n_y\in\mathbb{Z}} \psi_{approx.}(d(\mathbf{x}_{neur,i}, \mathbf{x}_{neur,i} + L \cdot (n_x, n_y))) \tag{66}$$

Note that the shift was applied to the second position. Theoretically, n_x,n_y is iterated over all integers and in this case it is irrelevant whether to shift the first or the second position. For numerical calculations however, the shift was applied to the second position.
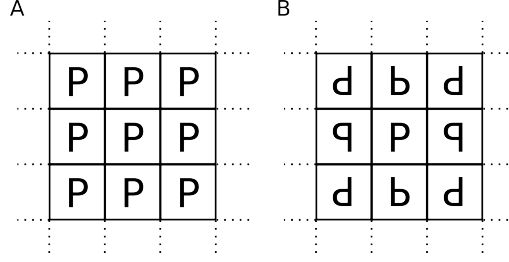
Figure 12: Sketch for patches of copied (and mirrored) positions for periodic (A) and Neumann (B) boundary conditions.

For the Neumann boundary condition, one finds

$$\psi_{ij,neum.} = \sum_{n_x,n_y \in \mathbb{Z}} \psi_{approx.} \left(d(\mathbf{x}_{neur,i}, M(\mathbf{x}_{neur,i}) + L \cdot (n_x, n_y)) \right) \tag{67}$$

$$M(\mathbf{x}) \equiv \begin{pmatrix} (-1)^{n_x} & 0 \\ 0 & (-1)^{n_y} \end{pmatrix} \mathbf{x} + L \cdot (mod(|n_x|, 2), mod(|n_y|, 2)) \tag{68}$$

We compared the firing rate distributions acquired from the solution of the random matrix system and those of the full simulated network by means of its standard deviation and skewness. While the standard deviation appears to be better fitting the full network in the case of Neumann boundary conditions, the prediction of skewness is more accurate for periodic boundaries. In both versions, the standard deviation seems to be underestimated by the solution of the random matrix equation. This seems reasonable, considering the fact that a network of irregularly spiking neurons "naturally" provides a certain amount of firing rate variability and that during simulation, all plasticity mechanisms where kept in place (changes of presynaptic weights requires an adjustment of the internal threshold to maintain the desired firing rate).

4.1.3 Mean-Field Approximation for the Variance of Firing Rates

Generally, Mean-Field approximations reduce the calculation of a full set of interacting entities (or particles, in the context of physics) to a single instance interacting with an effective mean of the entire field, especially ignoring the influence of the single instance onto the whole set of entities and thus the field itself.

In the system presented here, a single neuron with a firing rate ν must fulfil the equation

$$\nu = \frac{NO_0 - \sum_i \nu_i \psi(d_i)}{\psi_0} \tag{69}$$

where i indexes over all "remaining" neurons and d_i refers to the euclidean distance of the sample neuron to "field"-neuron i. ψ_0 is the factor that - multiplied with ν - yields the NO-concentration at the origin of the sample neuron.

Depending on the constraints that one imposes onto the system, one might look for different properties to be extracted from this equation. Specifically, in the simulation protocol that has been used in all previous simulations, the average firing rate was forced to a certain value by means of adjusting the target concentration NO_0. A Mean-Field approximation for the average firing rate therefore is of no relevance in this particular case.
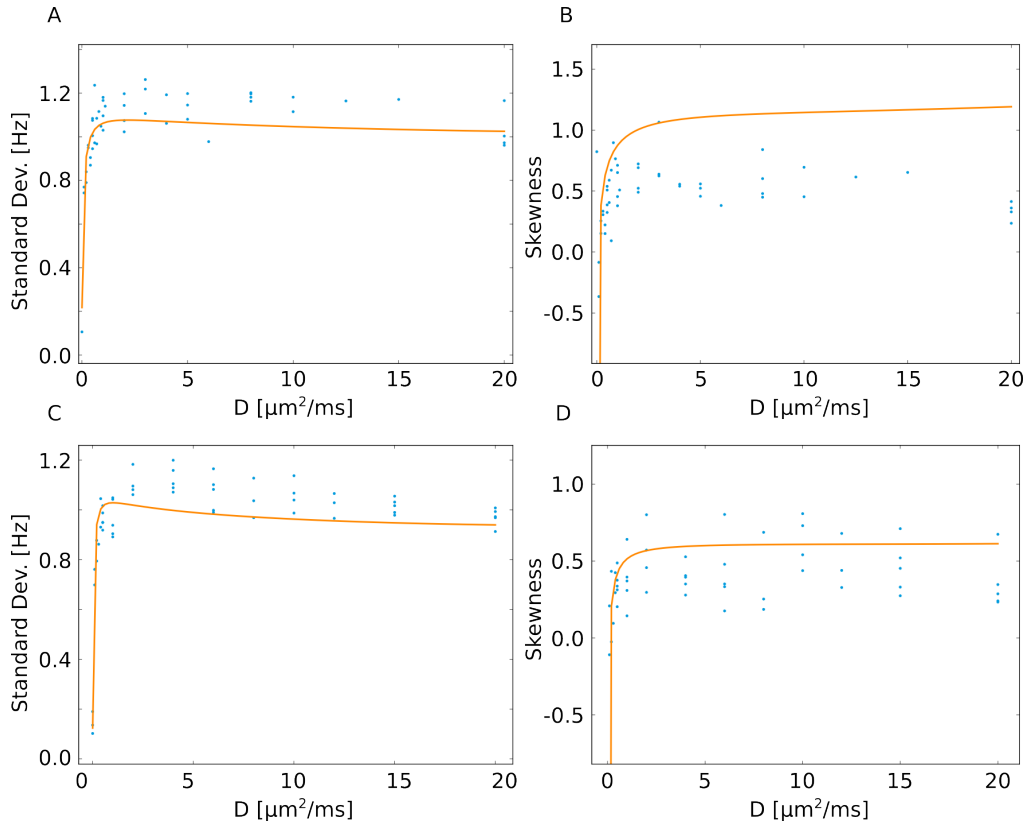
Figure 13: Standard deviation and skewness of firing rate distributions for the full spiking network (blue) and the solution of the random matrix model (orange) for Neumann (A,B) and periodic (C,D) boundary conditions.

However, one might try to give an estimate for the variance of the firing rate distribution in dependence of the diffusion constant D. Interpreting ν in (69) as a stochastic variable, one finds

$$Var[\nu] = \frac{Var[\sum_i \nu_i \psi(d_i)]}{\psi_0^2} \tag{70}$$

As an approximation, one can now replace all ν_i by the mean activity, which has been forced to a certain value ν_0:

$$Var[\nu] = \frac{\nu_0^2 \cdot Var[\sum_i \psi(d_i)]}{\psi_0^2} \tag{71}$$

The random individual neurons' positions are statistically independent, therefore one gets

$$Var[\nu] = \frac{\nu_0^2 \cdot N \cdot Var[\psi(d)]}{\psi_0^2} \tag{72}$$

where N is the number of neurons. One should note however that this expression only applies to the case of open boundaries. Furthermore, depending on the position of the "sample neuron" relative to the population, one can achieve different statistics for $\psi(d)$. The limit case, in which both remarks are of no relevance, is a population of a certain density spreading across a tissue of infinite size.

References

[1] Daniel Miner and Jochen Triesch. Plasticity-driven self-organization under topological constraints accounts for non-random features of cortical synaptic wiring. *PLoS Computational Biology*, 2016.

[2] Yann Sweeney, Jeanette Hellgren Kotaleski, and Matthias H. Hennig. A diffusive homeostatic signal maintains neural heterogeneity and responsiveness in cortical networks. *PLoS Computational Biology*, 2015.

[3] Romain Brette, Dan Goodman, and Marcel Stirnberg. The brian spiking neural network simulator (version 1.0) [computer software]. `http://www.briansimulator.org/`, 2016.

[4] Li I. Zhang, Li I. Zhang, Huizhong W. Tao, Christine E. Holt, William A. Harris, and Mu-ming Poo. A critical window for cooperation and competition among developing retinotectal synapses. *Nature*, 395:37–44, 1998.

[5] Guo-qiang Bi and Mu-ming Poo. Synaptic modifications in cultured hippocampal neurons: Dependence on spike timing, synaptic strength, and postsynaptic cell type. *The Journal of Neuroscience*, 18(24):10464–10472, 1998.

[6] Robert C. Froemke, Mu-ming Poo, and Yang Dan. Spike-timing-dependent synaptic plasticity depends on dendritic location. *Nature*, 434(7030):221–225, March 2005.

[7] Henry Markram, Yun Wang, and Misha Tsodyks. Differential signaling via the same axon of neocortical pyramidal neurons. *Proceedings of the National Academy of Sciences*, 95(9):5323–5328, 1998.

[8] Barry W. Connors and Michael J. Gutnick. Intrinsic firing patterns of diverse neocortical neurons. *Trends in Neurosciences*, 13(3):99 – 104, 1990.

[9] Jan Benda and Andreas V. M. Herz. A universal model for spike-frequency adaption. *Neural Computation*, 15(11):2523–2564, 2003.

[10] Niraj S. Desai, Lana C. Rutherford, and Gina G. Turrigiano. Plasticity in the intrinsic excitability of cortical pyramidal neurons. *Nature Neuroscience*, 2:515–520, 1999.

[11] Eugene M. Izhikevich. *Dynamical Systems in Neuroscience - The Geometry of Excitability and Bursting*. The MIT Press, 2007.

[12] Richard G. Knowles and Salvador Moncada. Nitrix oxide synthases in mammals. *Biochemical Journal*, 298(Pt 2):249–258, 1994.

[13] Richard G. Knowles, Miriam Palacios, Richard M. J. Palmer, and Salvador Moncada. Foneurons of nitric oxide from l-arginine in the central nervous system: A transduction mechanism for stimulation of the soluble guanylate cyclase. *Proceedings of the National Academy of Sciences*, 86:5159–5162, 1989.

[14] Bertil Hille. *Ionic Channels of Excitable Membranes*. Sinauer Associates, 2001.

[15] Joern R. Steinert, Cornelia Kopp-Scheinpflug, Claire Baker, R.A. John Challiss, Raj Mistry, Martin D. Haustein, Sarah J. Griffin, Huaxia Tong, Bruce P. Graham, and Ian D. Forsythe. Nitric oxide is a volume transmitter regulating postsynaptic excitability at a glutamatergic synapse. *Neuron*, 60(4):642 – 656, 2008.

[16] Hans-Christian Pape and Ralph Mager. Nitric oxide controls oscillatory activity in thalamocortical neurons. *Neuron*, 9:441–448, 1992.

[17] Peter Dayan and L.F. Abbott. *Theoretical Neuroscience*. MIT Press, 2001.

[18] AV. Hill. The possible effects of the aggregation of the molecules of haemoglobin on its dissociation curves. *The Journal of Physiology*, 40:iv—vii, 1910.

[19] Morris W. Hirsch and Stephen Smale, editors. *Differential Equations, Dynamical Systems, and Linear Algebra*, volume 60 of *Pure and Applied Mathematics*. Elsevier, 1974.

[20] Wulfram Gerstner. Time structure of the activity in neural network models. *Phys. Rev. E*, 51:738–758, Jan 1995.